Journal of Polymer Science

WILEY

JOURNAL OF POLYMER SCIENCE

RESEARCH ARTICLE OPEN ACCESS

Carbon Fiber-Reinforced Silicon Carbide (C/C-SiC) Fabrication Derived From Polyetherketoneketone (PEKK) as an Alternative Thermoplastic Carbon Precursor

Melissa Moos[1] | Jalena Best[1] | Stefan Flauder[1] | Steve R. Nutt[2] | Nico Langhof[1] | Stefan Schafföner[1,3,4]

[1]Chair of Ceramic Materials Engineering, University of Bayreuth, Bayreuth, Germany | [2]Department of Chemical Engineering and Materials Science and M. C. Gill Composites Center, University of Southern California, Vivian Hall of Engineering, Los Angeles, California, USA | [3]Bayreuth Center for Materials Science and Engineering, University of Bayreuth, Bayreuth, Germany | [4]Bavarian Polymer Institute, Bayreuth, Germany

Correspondence: Melissa Moos (melissa.moos@uni-bayreuth.de)

Received: 15 January 2025 | **Revised:** 24 March 2025 | **Accepted:** 27 March 2025

Keywords: mechanical testing | microstructural analysis | PEEK | PEKK | thermoplastic-derived C/C-SiC

ABSTRACT

This study shows the first successful fabrication of a carbon fiber-reinforced silicon carbide (C/C-SiC) via the liquid silicon infiltration process using two thermoplastic polyetherketoneketone (PEKK) powders as carbon precursors. Samples are analyzed after each processing step and compared to polyetheretherketone (PEEK)-derived reference samples. The carbon yield was above 65% for PEKK and 54% for PEEK, possibly due to the greater crosslinking potential of PEKK. Rheological measurements showed a higher melt viscosity of PEKK 60/40 (which consists of 60% terephtalic and 40% isophtalic moieties) than PEEK. The higher viscosity of PEKK 60/40 affected the carbon fiber-reinforced plastic (CFRP) microstructure because it resulted in more matrix pores and some partly saturated fiber tows in the PEKK 60/40-derived CFRP. The incomplete infiltration of fiber tows by PEKK in the CFRP state led to the undesirable reaction of the single carbon fibers during final siliconization. However, the effect was of minor influence, and the microstructure and phase composition remained unaffected. Mechanical testing of PEEK- and PEKK-derived C/C-SiC showed excellently comparable properties with a mean flexural strength above 200 MPa and a strain to failure above 0.55%. Thus, PEKK-derived C/C-SiC is a suitable alternative thermoplastic polymer for C/C-SiC fabrication.

1 | Introduction

C/C-SiC (carbon fiber-reinforced silicon carbide) is a ceramic matrix composite (CMC) consisting of carbon fibers in a matrix component of silicon carbide (SiC), silicon, and carbon. The main commercial application today is ceramic brake discs [1, 2] but the material is also used in the aerospace sector [3]. For example, it is integrated into the Orion Launch Abort System [4].

C/C-SiC CMCs can be fabricated using a three-step liquid silicon infiltration (LSI) process. In this process, a carbon fiber-reinforced polymer (CFRP) is first manufactured. Pyrolysis of this green body leads to the conversion of the polymer to non-graphitizable carbon, thus creating a porous carbon fiber-reinforced carbon (C/C) with a distinctive crack pattern. Finally, liquid silicon is added to infiltrate the network of cracks and pores at high temperatures, reacting with the carbon to produce a C/C-SiC [5–8]. The network cracks in the C/C strongly affect the microstructure and thus the mechanical properties of the C/C-SiC.

Multiple factors determine the crack networks, starting with the choice of the matrix polymer. For example, the char yield and the thermal properties of the polymer both influence the evolution of cracks during this process [9, 10]. To fabricate C/C-SiC, the matrix polymer must meet certain requirements, including acceptable fiber-matrix bonding and a low mass loss of the polymer after pyrolysis [3]. Additionally, the viscosity must

be sufficiently low to completely infiltrate the carbon fiber tows [11, 12]. For these reasons and because of the low cost of phenolic, phenolic resin is the most widely used carbon precursor for LSI fabrication of C/C-SiC [3, 9, 12].

The use of phenolic resin is not without drawbacks, however. For example, phenolics typically possess a relatively short shelf life and lack recyclability. Using recycled materials instead of primary materials is one factor in reducing the overall energy demand for C/C-SiC fabrication, making C/C-SiC more environmentally friendly. Furthermore, phenolic formulations contain solvents and thus require long curing times and low heating rates for pyrolysis [9]. Phenolics also undergo polycondensation reactions during curing, often leading to pore formation in the CFRP [9, 13]. These issues can be avoided by the use of selected thermoplastics [14–16].

Most standard and technical thermoplastics simply do not produce sufficient residual carbon (char yield), their melt viscosity is too high, or they lack a suitable fiber-matrix bonding. For example, one report described the pyrolysis of high-performance thermoplastics, such as polyamidimide (PAI) and polyetheretherketone (PEEK) [17]. Both polymers yielded a residual mass of > 45% after pyrolysis, but the high melt viscosity of PAI led to a partial tow infiltration and resulted in lower bending strength. By contrast, PEEK-derived C/C-SiC exhibited greater mechanical properties [13, 17].

PEEK belongs to the group of polyaryletherketones (PAEK). Another member of this group is polyetherketoneketone (PEKK) [18]. However, the structure of PEKK differs from that of PEEK. PEEK consists of two ether and one ketone group, while PEKK consists of only one ether and two ketone groups. Furthermore, the structure of PEKK can be tailored. As displayed in Figure 1, PEKK contains both a terephthalic and an isophthalic moiety. Thus, the terephthalate consists of a para isomer, and the isophthalate consists of a meta isomer. The meta isomers constitute a disruption or defect in the crystalline packing and thus influence the structural and thermal properties of the material, such as decreasing the degree of crystallinity and the melting point [19–22].

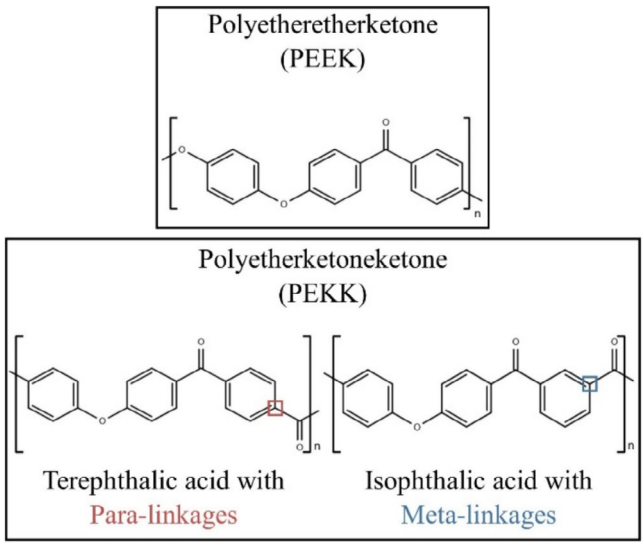

FIGURE 1 | Chemical structure of PEEK and PEKK.

By adjusting the terephthalic/isophthalic (T/I) ratio, the material can be adapted to the desired application. Because of this versatility, PEKK is not only used in high-performance applications, such as aviation, but also in the automotive sector [20, 21, 23, 24].

As described above, producing C/C-SiC CMCs via LSI requires using polymers with a high char yield [3]. Previous studies reported a carbon yield for PEKK of around 60%, making PEKK a promising candidate as a carbon precursor [12, 25]. One challenge, specifically concerning the C/C-SiC fabrication based on thermoplastics, stems from the possibility of re-melting of the thermoplastic during pyrolysis and the potential loss of dimensional stability. The phenomenon can be avoided by crosslinking the thermoplastic before pyrolysis [26]. However, crosslinking of PEEK-derived CFRP is a lengthy process [26]. Previous studies reported an increased molecular weight of PEKK compared to PEEK at 400°C and air, and thus asserted that PEKK possessed a greater capacity to develop crosslinks [27, 28]. Therefore, replacing PEEK with PEKK is a viable means to decrease the crosslinking time, making the process more efficient and sustainable. Thus, from this point of view, PEKK is an interesting polymer for C/C-SiC fabrication via LSI. However, the high melt viscosity of PEKK could pose challenges, potentially preventing complete saturation of the fiber tows and leading to a reaction of carbon fibers with liquid silicon during the LSI process [29–31].

To the best of our knowledge, there have been no reports to date of efforts to fabricate C/C-SiC using PEKK as the matrix material for CFRP production. The aim of the present work is to investigate the possibility of using PEKK as an alternative thermoplastic carbon precursor for LSI fabrication of C/C-SiC for the first time. The study assesses the influence of PEKK on the microstructure and properties of the final CMC. To achieve this goal, the raw materials were evaluated, and microstructural development was monitored during the production of CFRP, C/C, and C/C-SiC, including porosity, crack patterns, and phase distribution. Mechanical testing of C/C-SiC was conducted. The processing to and performance of the PEKK-derived C/C-SiC was compared to the processing and final properties of PEEK-derived C/C-SiC, whose successful fabrication has already been proven in previous studies [5, 9, 26, 32].

2 | Materials and Methods

Figure 2 gives an overview of the research methodology used in this study. A CFRP was fabricated via compression molding using carbon fibers and different thermoplastic polymers. The CFRP was then processed into a C/C-SiC using the liquid silicon infiltration method. The thermal properties of the raw materials, as well as the microstructure of the CFRP, C/C, and C/C-SiC were investigated. Additionally, C/C-SiC samples were mechanically tested.

2.1 | Raw Materials and C/C-SiC Preparation

The properties of C/C-SiC depend strongly on the constituent materials used for CFRP fabrication. For the present study, plain-weave carbon fibers with an areal weight of 245 g m^{-2} were chosen (HTA40 E13 3k, Teijin Carbon Europe GmbH,

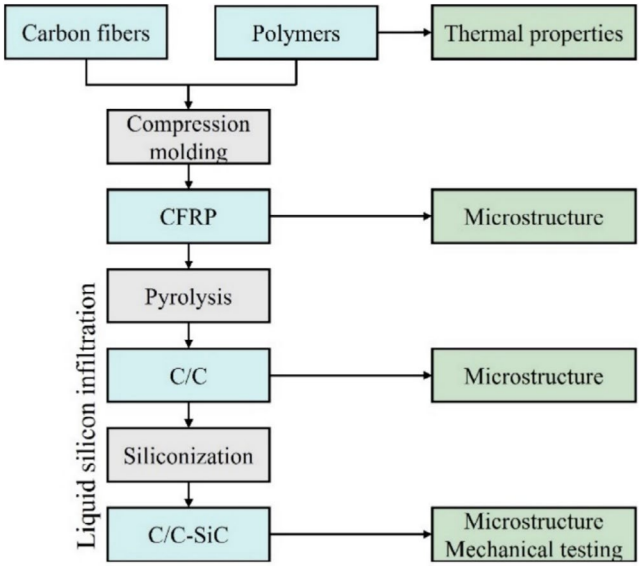

FIGURE 2 | Flow chart of research methodology.

Germany). Previous works showed enhanced mechanical properties of PEEK-derived C/C-SiC after a thermal pretreatment of the carbon fibers at 700°C [33]. Thus, the carbon fibers were pretreated in a nitrogen atmosphere at 700°C before CFRP fabrication. For the CFRP matrix material, three thermoplastic variants were used – (a) 6003PT PEKK powder with a T/I ratio of 60/40, (b) 7003PT PEKK powder with a T/I ratio of 70/30 (both Arkema Group, France) and (c) PEEK powder (KT880FP, Solvay, Belgium).

Four CFRP plates ($150 \times 150 \times 3\,mm^3$) for each of the three polymer precursors were fabricated by compression molding. Carbon fiber fabrics and polymer powders were alternately placed into a mold and compression molded at 400°C and $2\,N\,mm^{-2}$. Constituent proportions were selected to achieve a CFRP fiber volume fraction (FVF) of 50%.

Molded CFRP plates were processed using a liquid silicon infiltration process. Plates were pyrolyzed above 900°C in an inert gas atmosphere in a batch furnace (FCT Anlagenbau GmbH, Germany). Finally, the pyrolyzed C/C plates were siliconized under vacuum, using pure silicon (> 99.70 wt. %, Elkem As, Norway) and a batch furnace was set to a temperature above 1420°C (FCT Anlagenbau GmbH, Germany).

2.2 | Thermal Analysis

For the CFRP fabrication, it is vital to measure the melting point (T_m) and the glass transition temperature (T_g) of the polymeric matrix materials. Differential scanning calorimetry (DSC, DSC 1 Star System, Mettler Toledo, USA) was performed on the carbon precursors in a nitrogen atmosphere using an aluminum crucible with a lid. The heating rate was $10\,K\,min^{-1}$ from either 20°C to 320°C (1st heating cycle) for PEKK 60/40 or from 20°C to 360°C for PEKK 70/30 and PEEK. The different heating cycles were necessary to avoid any structural changes of the polymers, while ensuring to have passed the respective melting temperatures. This segment was followed by an isothermal dwell for 5 min. Samples were cooled to 100°C at $10\,K\,min^{-1}$ and held for 5 min (first cooling cycle). Afterwards, samples were subsequently heated to 400°C at $10\,K\,min^{-1}$ (second heating cycle). Data from the second heating cycle was used to determine the glass transition temperature and the melting point. The glass transition temperature was defined by the inflection point of the respective step and the melting temperature by the maximum of the respective peak.

Char yields after pyrolysis were determined for the three polymers using thermogravimetric analyzes (TGA, STA 449F5 Jupiter, Netzsch GmbH & Co. Holding KG, Germany). All three carbon precursors were placed in a closed Al_2O_3 crucible and heated from room temperature to 1000°C in flowing nitrogen ($70\,mL\,min^{-1}$). The heating rate was either $10\,K\,min^{-1}$ or simulated the scheme used for pyrolysis of the CFRP.

2.3 | Rheology

The melt viscosity is vital for a sufficient fiber tow infiltration and was analyzed using a rheometer (AntonPaar MCR 702, Anton Paar Group AG, Switzerland). To avoid trapped air during the rheological measurements, platelets with a diameter of 25 mm were fabricated using the compression molding process and a maximum temperature of 360°C. The rheological measurements were carried out at 400°C. This temperature was chosen to imitate the compression molding process. To prevent oxidation of the samples, measurements were conducted in a nitrogen atmosphere. A plate-cone geometry was used with a diameter of 25 mm and an angle of 1°.

2.4 | Fiber Volume Fraction, Density and Porosity

The amount of carbon fibers within a composite plays a key role when it comes to its mechanical properties. Hence, the prepared samples needed a comparable fiber volume fraction. The fiber volume fraction in the CFRP, C/C, and C/C-SiC state was calculated by dividing the volume of the plain-weave carbon fiber layers through the volume of the plate. Thus, the length and width, as well as the thickness of the plates were measured for CFRP, C/C, and C/C-SiC conditions. After each processing step, open porosity and bulk density were investigated by the Archimedes method (DIN EN ISO 18754:2020).

2.5 | Analysis of the Microstructure

The microstructure after each processing step was analyzed by light microscopy of polished sections (DSX1000, Olympus K.K., Japan). Crack widths and crack densities were determined from a minimum of four stitched images for each C/C material. Each image covered a surface area of at least $7.5\,mm^2$. Using the image analysis software "Dragonfly" (Version 2022.2.0.1409, Comet Technologies Canada Inc., Canada), a deep learning model based on semantic segmentation was trained to analyze the crack width. The software identified cracks and measured the minimal feret diameter. Every width from 2.5 to 50 µm was identified as a valid crack width. Crack density was calculated as the number of cracks divided by the area of the analyzed image.

Phase analysis—to determine the different amounts of carbon, silicon carbide and silicon of the different C/C-SiC samples—was conducted by two methods. First, analysis of images from a light microscope was performed using the deep learning module ("Dragonfly"). At least seven samples of the PEKK 60/40-, PEKK 70/30 and PEEK-derived C/C-SiC variants were extracted for preparation of polished sections. Roughly 100 images of each C/C-SiC type were recorded, each image covering an area of about 1 mm^2. Image analysis was performed using the same deep learning module based on semantic segmentation on exemplary images. Six classes were determined for training: "carbon matrix", "carbon fibers in 90° direction", "carbon fibers in 0° direction", "silicon", "silicon carbide" and "pores".

To augment the image analysis, a second method was employed to analyze the phase composition. Carbon was first removed by oxidizing the different C/C-SiC samples, then helium pycnometry was used to measure the density of the remaining Si-SiC. To increase the surface-to-volume ratio, the C/C-SiC samples were ground (Pulverisette 9, Fritsch GmbH, Germany) two times for 30 s to produce a fine powder with a high surface-to-volume ratio to facilitate the oxidation of the C/C-SiC. From each C/C-SiC variant, samples from three different plates were used. After grinding, the powder was oxidized in air with a heating rate of 10 K min^{-1}, a maximum temperature of 900°C, and held for 60 min. Those parameters were chosen to ensure the reaction of carbon to CO_2. Before and after oxidation, samples were weighed and the carbon content C_{Carbon} calculated according to Equation (1).

$$C_{Carbon} = \frac{m_{C,before} - m_{C,end}}{m_{C,before}} \cdot 100\,\% \quad [\text{wt. \%}] \tag{1}$$

where $m_{C,before}$ and $m_{C,end}$ are the carbon mass before and after pyrolysis.

Next, the density of the remaining Si-SiC was measured using helium pycnometry. The amount of silicon (Si_{pyk}) and silicon carbide (SiC_{pyk}) in the mixture was calculated using Equations (2) and (3).

$$Si_{pyk} = \frac{\rho_{pyk} - \rho_{SiC}}{\rho_{Si} - \rho_{SiC}} \quad [\text{wt. \%}] \tag{2}$$

$$SiC_{pyk} = \frac{\rho_{pyk} - \rho_{Si}}{\rho_{SiC} - \rho_{Si}} \quad [\text{wt. \%}] \tag{3}$$

where ρ_{Pyk} is the density measured by helium pycnometry, and ρ_{Si} and ρ_{SiC} are the densities of silicon (2.3 g cm^{-3}) and silicon carbide (3.2 g cm^{-3}). Considering the amount of carbon oxidized, the silicon (C_{Si}) and the silicon carbide (C_{SiC}) content of the C/C-SiC were calculated according to Equations (4) and (5).

$$C_{Si} = \frac{\rho_{pyk} - \rho_{SiC}}{\rho_{Si} - \rho_{SiC}} \cdot \left(1 - \frac{C}{100}\right) \cdot 100\,\% \quad [\text{wt. \%}] \tag{4}$$

$$C_{SiC} = \frac{\rho_{pyk} - \rho_{Si}}{\rho_{SiC} - \rho_{Si}} \cdot \left(1 - \frac{C}{100}\right) \cdot 100\,\% \quad [\text{wt. \%}] \tag{5}$$

To compare the results with the image analysis results, values were converted to volume percent using 1.6 g cm^{-3} for the density of carbon ρ_{Carbon}. The silicon (Si), silicon carbide (SiC) and carbon (C) content in the C/C-SiC was calculated using Equations (6–8), respectively.

$$Si = \frac{\frac{C_{Si}}{\rho_{Si}}}{\frac{C_{Carbon}}{\rho_{Carbon}} + \frac{C_{Si}}{\rho_{Si}} + \frac{C_{SiC}}{\rho_{SiC}}} \tag{6}$$

$$SiC = \frac{\frac{C_{SiC}}{\rho_{SiC}}}{\frac{C_{Carbon}}{\rho_{Carbon}} + \frac{C_{Si}}{\rho_{Si}} + \frac{C_{SiC}}{\rho_{SiC}}} \tag{7}$$

$$C = \frac{\frac{C_{Carbon}}{\rho_{C}}}{\frac{C_{Carbon}}{\rho_{Carbon}} + \frac{C_{Si}}{\rho_{Si}} + \frac{C_{SiC}}{\rho_{SiC}}} \tag{8}$$

2.6 | Three-Point Bending Tests of C/C-SiC

Flexural strength, strain to failure, and Young's modulus were measured using a three-point bending test (Inspect table blue 1 kN, Hegewald & Peschke GmbH, Germany) according to DIN EN ISO 17138:2022–06. Roughly 60 samples of PEKK 60/40-, PEKK 70/30- and PEEK-derived C/C-SiC were tested using 10 mm wide and 3 mm thick beams with a length/thickness-ratio of more than 20. The traverse speed was 1 mm/min. The Young's modulus was determined between 0.05% and 0.25% deflection. Fracture surfaces were inspected using scanning electron microscopy (SEM, Sigma 300 VB, Zeiss AG, Germany) at 15 kV.

3 | Results and Discussion

The current state-of-the-art for LSI fabrication of C/C-SiC starts with CFRP based on phenolic resin [34–36]. However, mechanical properties can be boosted by substituting thermoplastics such as PEEK for phenolic resin matrices [32]. Nonetheless, thermoplastic polymers are rarely selected as polymer precursors for C/C-SiC. This work aims to investigate the fabrication of C/C-SiC derived from thermoplastic PEKK, starting with a thorough analysis of the neat polymer, followed by monitoring the three processing steps from the CFRP to the C/C-SiC. To meet this goal, analytical methods were used, followed by mechanical testing of the C/C-SiC.

3.1 | Differential Scanning Calorimetry

DSC (differential scanning calorimetry) results from the second heating cycle reveal differences in the three powder formulations (Figure 3). After the second heating cycle, a step appeared at 147°C for PEEK, 159°C for PEKK 70/30, and 158°C for PEKK 60/40. The steps represent values of the glass transition temperature for the polymers. Keto linkages are less flexible than ether linkages, leading to an enhanced chain rigidity of the molecule, which increases the glass transition temperature [20]. Thus, the higher glass transition temperatures for PEKK 60/40 and PEKK 70/30 were attributed to the greater amount of ketone groups compared to PEEK.

Peaks for PEEK and PEKK 70/30 at 343°C–344°C and at 300°C for PEKK 60/40 signified the melting point for the thermoplastics. As

described previously, the orientation of the ketone groups within the molecules can be tailored. In particular, when the amount of isophthalate moieties is increased, the crystalline structure of the polymer is influenced and impacts the thermal properties [20]. Thus, the melting point of PEKK 60/40 was lower, and the melting point for PEKK 70/30 was in the same range as for PEEK [19, 20].

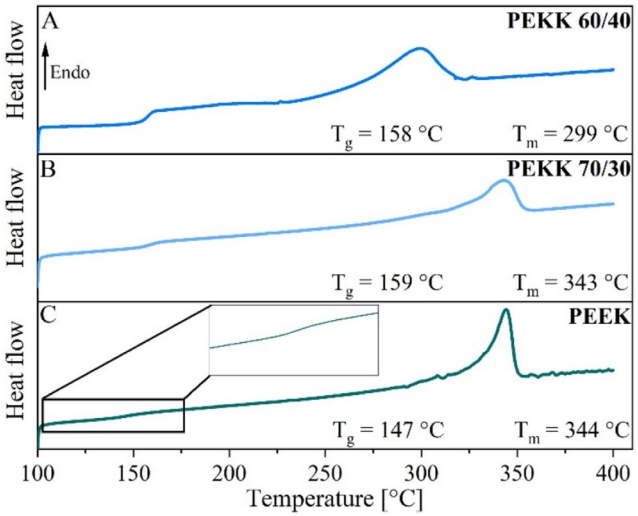

FIGURE 3 | Differential scanning calorimetry of (A) PEKK 60/40, (B) PEKK 70/30, and (C) PEEK. The glass transition temperature and the melting point of the three polymers were determined.

3.2 | Thermogravimetric Analysis

The mass of PEKK 60/40, PEKK 70/30, and PEEK during pyrolysis as a function of the temperature is shown in Figure 4A for a heating rate below 5 K min^{-1} and Figure 4B for a heating rate of 10 K min^{-1}. Figure 4C and Figure 4D depict the derivative of the data from Figure 4A,B. $T_{95\%}$ is the temperature at which the polymer experienced a weight loss of 5% and is defined in this work as thermal stability. All polymers experienced one major step of decomposition, and a higher heating rate resulted in a greater $T_{95\%}$ for the three samples. However, PEKK 60/40 had the lowest $T_{95\%}$, followed by PEKK 70/30 and PEEK. PEKK 60/40 exhibited a residual mass after pyrolysis of 66.2%, PEKK 70/30 of 65.1% and PEEK of only 53.8% when a heating rate below 5 K min^{-1} was applied. Note that for the three polymers, the residual mass was reduced using a greater heating rate. For this scenario, the char yield of PEKK 60/40 and PEKK 70/30 decreased to 60.4% and 56.7%, respectively, while for PEEK the char yield was 51.9%.

Previous works attributed the major decomposition step to thermal degradation due to random chain scission [37]. It was also indicated that the development of crosslinks increases the char yield [22]. This aligns well with the results from this work, since lower thermal stability and lower heating rates resulted in a longer time span for crosslinking, leading to greater char yields.

The greater residual mass of PEKK 60/40 compared to PEKK 70/30 was reported in previous studies, which posited

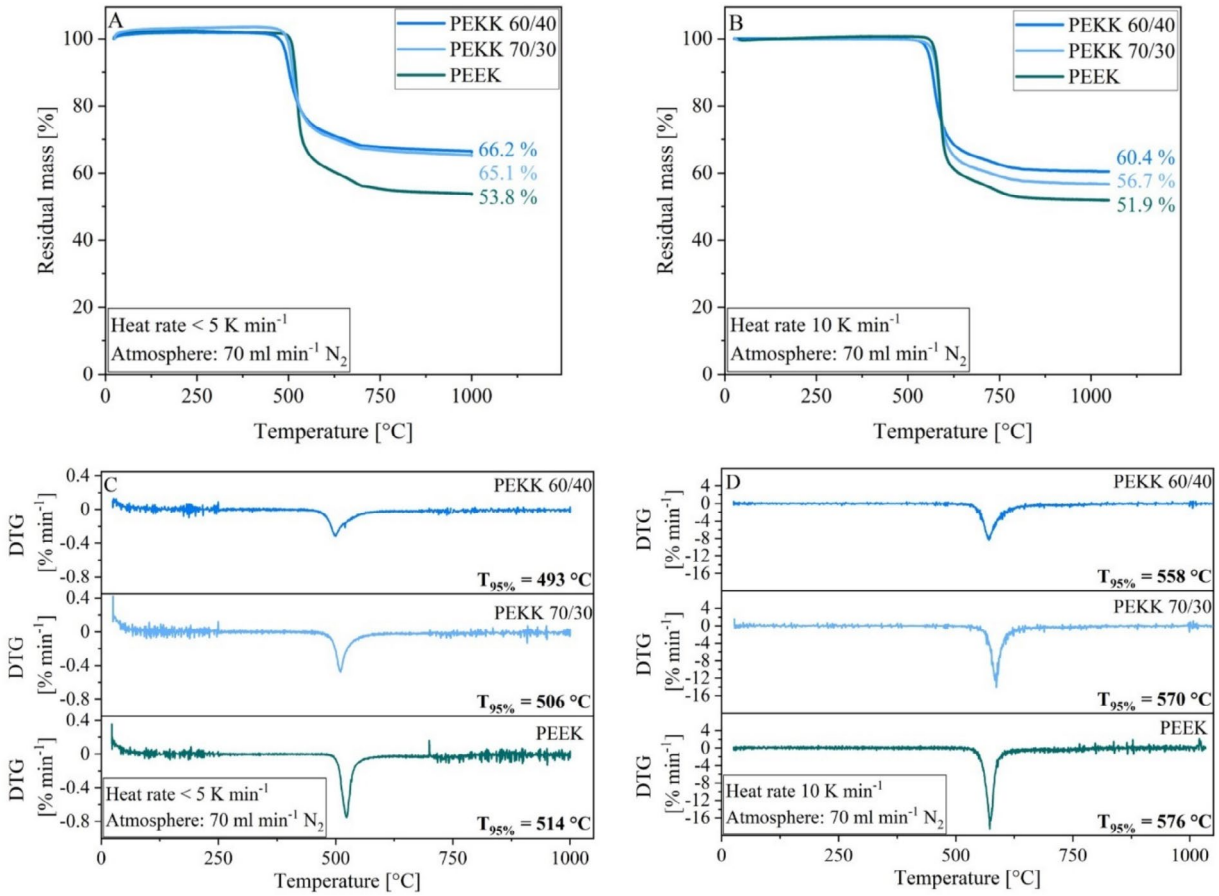

FIGURE 4 | Thermogravimetric analysis of PEKK 60/40, PEKK 70/30, and PEEK powder with (A) a heating rate below 5 K min^{-1} and (B) of 10 K min^{-1} under nitrogen. (C) depicts the first derivative of (A) and (D) the first derivative of (B).

that the primary difference between the two formulations was their T/I ratio [38]. The study hypothesized that a lower T/I ratio produces a higher crosslink density and, just as Rashed et al. and Vielle et al. [22, 37] they also postulated that increased crosslinking results in an enhanced char yield [38]. This hypothesis is supported by another study [27], which reported an exponential increase in viscosity over time at temperatures above 380°C for PEKK 60/40 and attributed the behavior to crosslinking reactions [27]. Additionally, the normalized viscosity over a time span of 3 h at 380°C for PEKK 70/30 and PEKK 60/40 was investigated in reference [38]. After 3 h, the viscosity of PEKK 60/40 increased 90 times, compared to only 25 times of PEKK 70/30 [38]. This is an indicator that PEKK 60/40 shows enhanced crosslinking, which might also result in higher char yield compared to PEKK 70/30.

To date, there have been no reports explaining the greater residual mass of PEKK compared to PEEK. However, the mechanism proposed by the mentioned studies for the pyrolysis behavior of PEKK could also interpret the differences in residual mass between PEEK and PEKK. Previous works compared changes in weight-average molar mass (M_w) and number-average molar mass (M_n) of PEEK and PEKK after 30 min in air at 400°C. Under these conditions, M_w of PEKK increased by 13% while the increase measured for PEEK was only 7%. M_n remained constant. The authors of this study attributed this to two intertwined mechanisms, which are crosslinking and chain scission. The greater increase of M_w of PEKK compared to PEEK implies an enhanced potential for the development of crosslinks concerning PEKK in air [27, 28]. Note that different authors also investigated crosslinking of PEEK and PEKK in nitrogen. They found that, although more extensively in oxygen atmospheres, crosslinking also occurs in nitrogen atmosphere [27, 28, 39]. This indicated that the greater residual mass of PEKK compared to PEEK can be attributed, at least in part, to increased crosslinking in PEKK. However, this assertion awaits further validation.

3.3 | Rheology

The viscosity of PEEK, PEKK 60/40, and PEKK 70/30 as a function of shear rate at 400°C is shown in Figure 5. All three formulations exhibited shear-thinning behavior, i.e., the viscosity decreased with increasing shear rate, and the differences in viscosity became negligible at shear rates $>100\,s^{-1}$. The shear-thinning behavior is attributed to de-entanglement of polymer molecules with increasing shear rates. At low shear rates, the viscosity of PEKK 60/40 was greater than PEKK 70/30, while PEEK exhibited the lowest viscosity. Interestingly, no Newtonian plateau was found at low shear rates for PEKK 60/40 and PEKK 70/30. Previous works investigated the normalized viscosity of PEKK 60/40 and PEKK 70/30 with respect to time at 380°C for 3 h [38]. The normalized viscosity in their work is defined as complex viscosity at a specific time divided by the initial viscosity. An exponential increase in normalized viscosity for both samples was found and explained with crosslinking processes. It can be calculated from their data that after 30 min, the normalized viscosity is 2.3 for PEKK 60/40 and 1.8 for PEKK 70/30 [38]. Another work investigated the complex viscosity of different

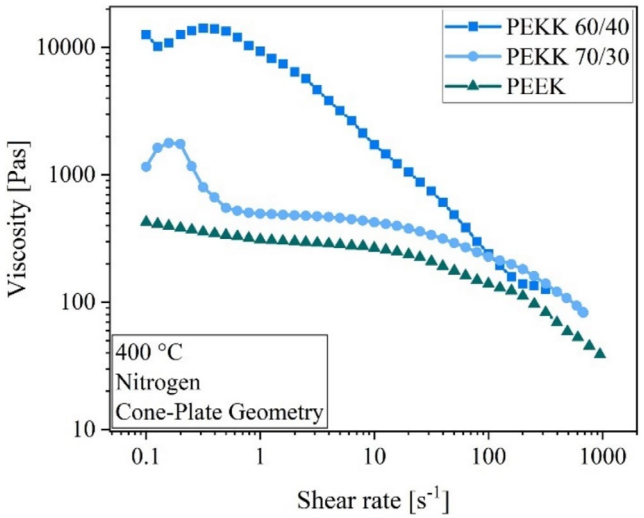

FIGURE 5 | Viscosity of PEKK 60/40, PEKK 70/30, and PEEK as a function of the shear rate at 400°C under nitrogen atmosphere.

commercial PEEK samples at 400°C for a duration of 30 min [39]. They found only a minor increase in complex viscosity for most of their tested PEEK samples. Thus, the absent Newtonian plateau for the two PEKK samples at low shear rates could be attributed to crosslinking of PEKK 60/40 and PEKK 70/30.

3.4 | Open Porosity and Fiber Volume Fraction

The fiber volume fraction (FVF) in the CFRPs was similar for PEKK 70/30 and PEEK (around 49%), while the fiber volume fraction for PEKK 60/40 was slightly less (around 47%), as shown in Figure 6A. Re-melting processes of the polymer matrix during pyrolysis led to an increase in the plate thickness and caused plates to delaminate. To prevent this delamination, a load was applied to the plate surfaces. The plate thickness still changed slightly during pyrolysis and affected the FVF. The FVF of PEKK 60/40 and PEKK 70/30 after pyrolysis was similar (48% and 49%, respectively). However, the FVF for PEEK-derived C/C increased to 51%. Assuming that there was no reaction of carbon fibers during siliconization, the theoretical FVF for PEKK 60/40-derived plates was the lowest (around 47%), while PEEK-derived C/C-SiC plates exhibited the highest theoretical FVF (around 51%).

Figure 6B plots the bulk densities of composites in CFRP, C/C, and C/C-SiC states as a function of the polymer precursor. The bulk density of PEKK 60/40-derived CFRP was $1.35\,g\,cm^{-3}$, much less than that of PEEK- and PEKK 70/30-derived CFRP, which yielded 1.43 and $1.45\,g\,cm^{-3}$, respectively. Additionally, the open porosity of PEEK, PEKK 60/40, and PEKK 70/30-derived CFRP, C/C, and C/C-SiC states was not affected by the polymer formulation, as shown in Figure 6C. For the CFRP state, the open porosity was between 5.6% and 6.4%. The similar open porosity for all three CFRP types supported the conclusion that the bulk density reflected a greater number of closed pores. Reasons for an increased closed porosity could either be closed pores within the matrix polymer or incompletely infiltrated fiber tows.

After pyrolysis, the open porosity increased as a result of mass loss and volume shrinkage of the polymer during conversion to carbon (Figure 6C). However, the open porosity for all C/C samples derived from different polymer types was around 23.5% – 26%. Such a minor difference is unexpected, because a higher residual mass after pyrolysis normally translates to a reduced porosity. Because the bulk density for all three C/C types was similar (1.18–1.21 g cm^{-3}), closed porosity values for the three materials were expected to be alike. However, as shown in Figure 6A, the FVF for PEEK-derived C/C increased during pyrolysis, accompanied by a decrease in plate thickness. The decrease in plate thickness possibly compensated for the difference in char yield and led to similar amounts of open pores.

As shown in Figure 6C, after siliconization, the open porosity for the three C/C-SiC types decreased to 5.5% – 5.7% due to the infiltration of the C/C with silicon and the subsequent reaction of carbon and silicon to form SiC. An increase in bulk density to 1.81–1.85 g cm^{-3} was measured, although there was no correlation between open porosity or bulk density and CFRP polymer type. However, similar bulk densities and values for open porosity are indicators for comparable phase compositions.

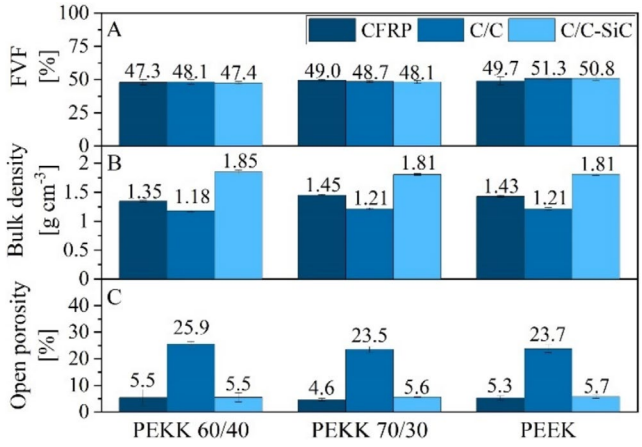

FIGURE 6 | (A) Fiber volume fraction, (B) bulk density, and (C) open porosity of the PEKK 60/40-, PEKK 70/30-, and PEEK-derived CFRP, C/C, and C/C-SiC.

3.5 | Microstructure

Microstructures of PEKK 60/40 (A)-, PEKK 70/30 (B)- and PEEK (C)-derived CFRP were revealed in polished sections, Figure 7. Transverse cracks were present in 0° fiber tows (see marking in Figure 7C), particularly in PEEK and to a smaller extent in PEKK 70/30. The tow cracks were less frequent in PEKK 60/40-derived CFRP. According to the respective data sheets and literature, the coefficient of thermal expansion for PEEK is consistent around $50\times10^{-6}\,K^{-1}$ and twice as high as the average CTE of PEKK 70/30 and PEKK 60/40 between −100°C and the glass transition temperature [40]. Additionally, the CTE of PEKK polymers is closer to the CTE of carbon fibers in the radial direction [41]. The greater CTE of PEEK probably caused increased shrinkage in PEEK-derived CFRP, stresses within the carbon fiber tows during cooling after compression molding, and increased crack density within the fiber tows. Furthermore, crystallization caused additional shrinkage of the polymers [42]. PEKK 60/40, a pseudo-amorphous thermoplastic, experienced less shrinkage than PEKK 70/30 and PEEK during cooling, resulting in fewer transversal cracks in PEKK 60/40-derived CFRP.

Note that for PEKK 60/40-derived CFRP, fiber tows often were not fully saturated (see marking in Figure 7A). Partially saturated fiber tows were rarely seen in PEKK 70/30- and PEEK-derived CFRP. Higher melt viscosity could have restricted the flow of polymer melts into the fiber tows. As shown in Figure 5, the greater melt viscosity of PEKK 60/40 compared to PEKK 70/30 and PEEK accounted for the lower level of tow saturation in PEKK 60/40-derived CFRP.

Finally, although matrix pores were present in all three CFRP types, PEKK 60/40 had a higher level of porosity than PEEK and PEKK 70/30. The increased matrix porosity in the PEKK 60/40-derived CFRP potentially was a consequence of the higher melt viscosity of PEKK 60/40, which limited the flow of the polymer melt during compression molding and hindered trapped gasses from escaping. The larger number of pores and incompletely saturated fiber tows in the PEKK 60/40-derived CFRP was consistent with the lower bulk density values depicted in Figure 6B.

The microstructures for PEKK 60/40 (A)-, PEKK 70/30 (B)- and PEEK (C)-derived C/C plates are shown in Figure 8. The

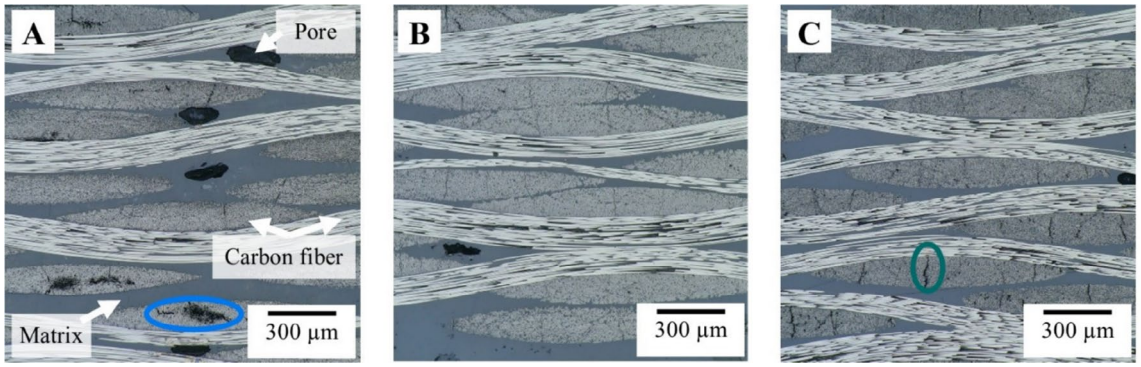

FIGURE 7 | Microstructure (bright field) of (A) PEKK 60/40-, (B) PEKK 70/30-, and (C) PEEK-derived CFRP. In (A), a partly infiltrated carbon fiber tow, and in (C) a vertical crack is marked.

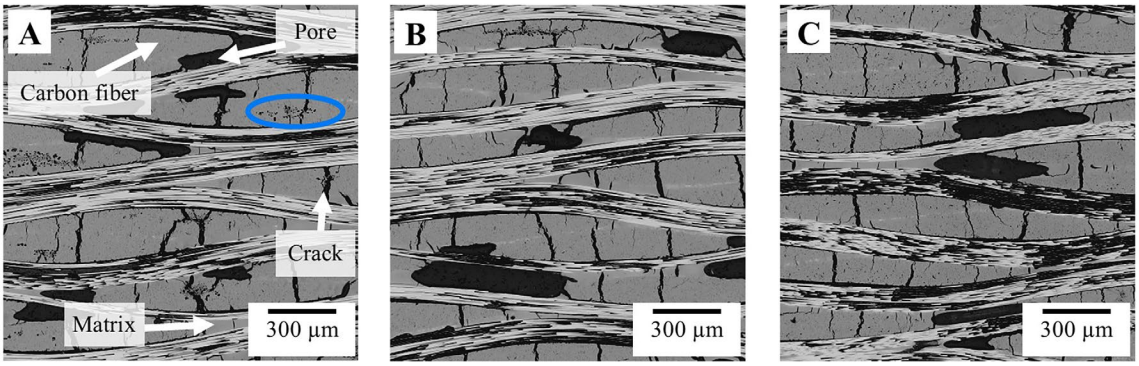

FIGURE 8 | Microstructure (bright field) of (A) PEKK 60/40-, (B) PEKK 70/30-, and (C) PEEK-derived C/C. In (A), an exemplary pore within the carbon fiber tow due to insufficient infiltration of the bundle in the CFRP is marked.

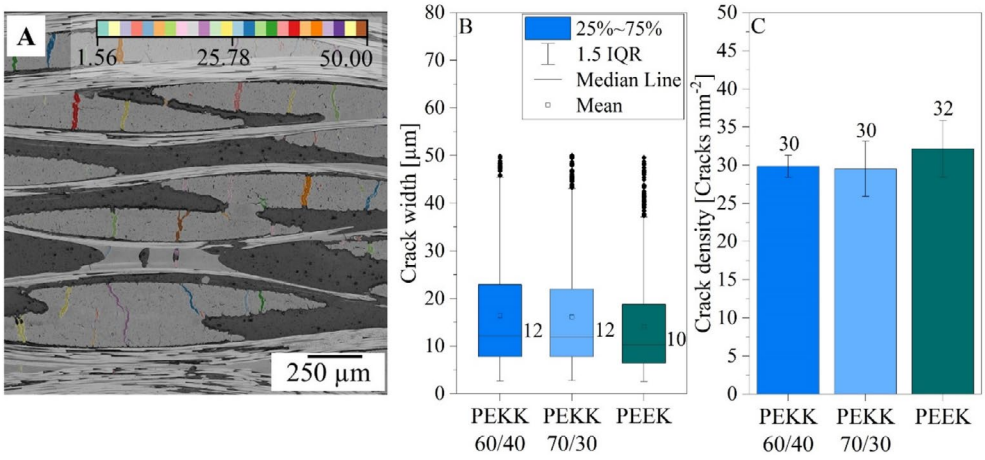

FIGURE 9 | (A) Exemplary image for crack width and crack density determination. (B) Resulting crack width and (C) crack density.

microstructure revealed a distinct, characteristic crack pattern, with cracks running transverse to the thin dimension of carbon fiber tows, known as segmentation cracks. All three C/C types also exhibited pores between some 0° and 90° fiber tows. Both phenomena are common to C/C composites [43]. Additionally, macro pores were present in the carbon matrix, which is typical for thermoplastic-derived C/C and has been reported elsewhere [44].

Pores within the carbon fiber tows were observed only in PEKK 60/40-derived C/C (see marking in Figure 8A). Intratow pores were caused by incomplete saturation of fiber tows during CFRP synthesis. Nonetheless, regardless of the polymer, fiber-matrix debonding was rare, indicating adhesion of the fibers and the matrix. Adhesion between carbon fibers and the carbon matrix is vital because only if they adhere to the matrix, carbon fibers are protected from liquid silicon during siliconization [45, 46].

Analysis of the cracks in PEKK 60/40-, PEKK 70/30-, and PEEK-derived C/C revealed mean widths of 10 – 12 µm and mean crack densities of 30 – 32 cracks mm^{-2} (Figure 9). Therefore, the crack pattern for all C/C variants was similar.

The microstructures of PEKK 60/40 (A, D)-, PEKK 70/30 (B, E)- and PEEK (C, F)-derived C/C-SiC are shown in Figure 10. Cracks (in the short transverse direction) in fiber tows were present in all three C/C-SiC variants. The different CTEs of silicon, silicon carbide, carbon fibers, and the carbon matrix caused thermal stresses during cooling after siliconization, leading to crack formation [33].

The C/C microstructure influenced and defined the C/C-SiC microstructure as well. Macropores (Figure 8) were filled with molten silicon during siliconization, forming silicon pools. Smaller cracks, such as segmentation cracks and the partial delamination cracks between fiber tows, were also filled with silicon, which reacted to some extent to form silicon carbide. Because the crack patterns for all three C/C variants were similar, the C/C-SiC microstructures exhibited negligible differences.

Closer inspection of the three C/C-SiC microstructures revealed SiC within the 0° fiber tows of PEKK 60/40-derived C/C-SiC. The incomplete polymer infiltration during CFRP manufacturing exposed carbon fibers to the silicon melt during siliconization, causing a (partial) reaction of fibers within the fiber tows to SiC (see marking in Figure 10D). This phenomenon was observed in the PEKK 60/40-derived C/C-SiC, but not in PEKK 70/30-derived or PEEK-derived C/C-SiC.

3.6 | Phase Analysis

Figure 11 is an image representative of C/C-SiC microstructures used to analyze the phase composition with an image analysis software ("Dragonfly"). The deep learning model detected

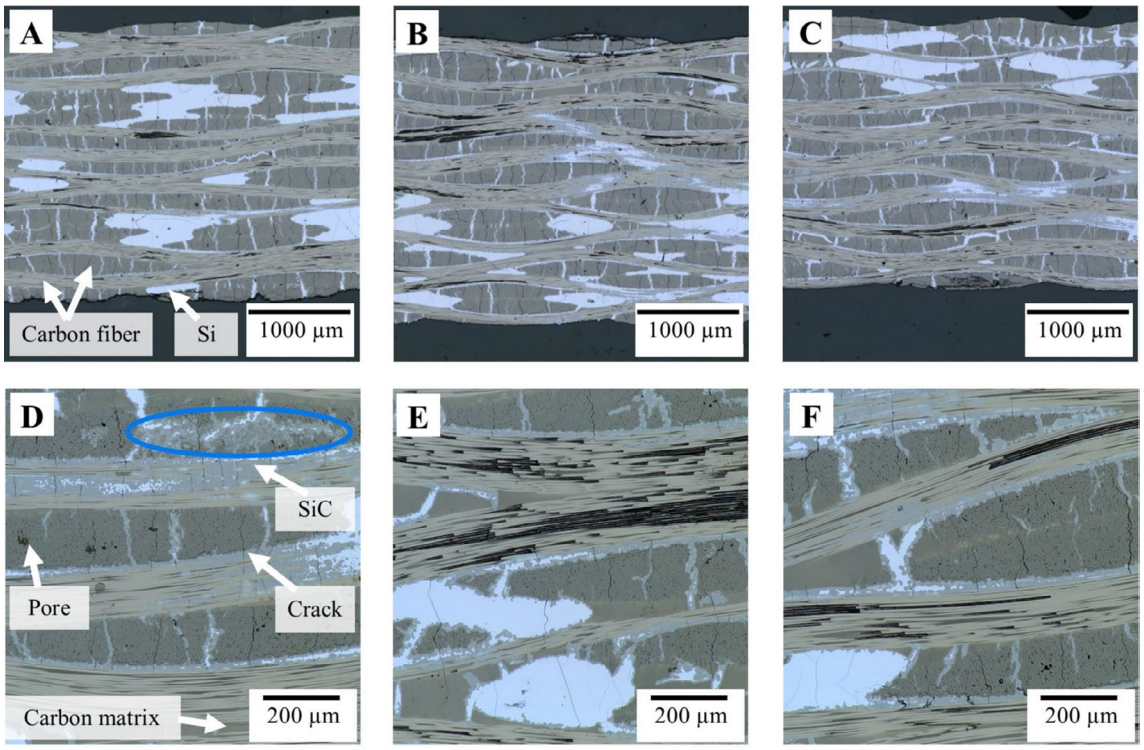

FIGURE 10 | Microstructure (bright field) of (A, D) PEKK 60/40-, (B, E) PEKK 70/30- and (C, F) PEEK-derived C/C-SiC. The blue marking in (A) highlights the reaction of single fibers within a bundle to SiC. The marking in (A) highlights the reaction of single carbon fibers within the bundle due to insufficient fiber tow infiltration in the CFRP.

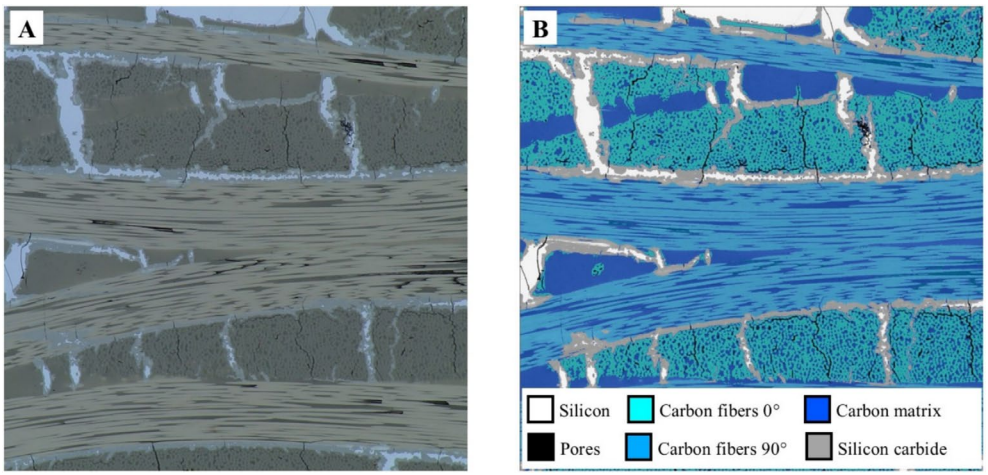

FIGURE 11 | Exemplary phase analysis image as generated with the deep learning tool "Dragonfly".

residual silicon (white), cracks and pores (black) with high accuracy. The software was used to detect SiC, but if the SiC was near or within a 90° fiber tow, the program sometimes mistook the SiC for 90° carbon fiber. The model identified 0° carbon fibers with some consistency, although in some cases, the carbon matrix was misidentified as 0° carbon fibers. To overcome this drawback, the carbon matrix, carbon fibers in 0° and 90° directions were summed and identified as "carbon content".

The volume fractions of silicon, SiC, and carbon are shown in bar charts in Figure 12A. Independent of the polymer, the carbon content in the three C/C-SiC was 71% – 73%, the silicon content was 12% – 15%, and the SiC content was 12% – 14%. All C/C-SiC types showed porosity of 2% – 4%. Hence, considering the standard deviation, no correlation between the CFRP matrix polymer and C/C-SiC phase composition was observed.

The results from the phase analysis by combination of oxidation and helium pycnometry are shown in Figure 12B. The carbon content for PEKK 60/40-, PEKK 70/30-, and PEEK-derived C/C-SiC was about 70%, the mean silicon content around 20%, and the mean silicon carbide content was 10% – 13%. Comparison of the two methods of phase analysis revealed similar amounts of carbon and of silicon carbide.

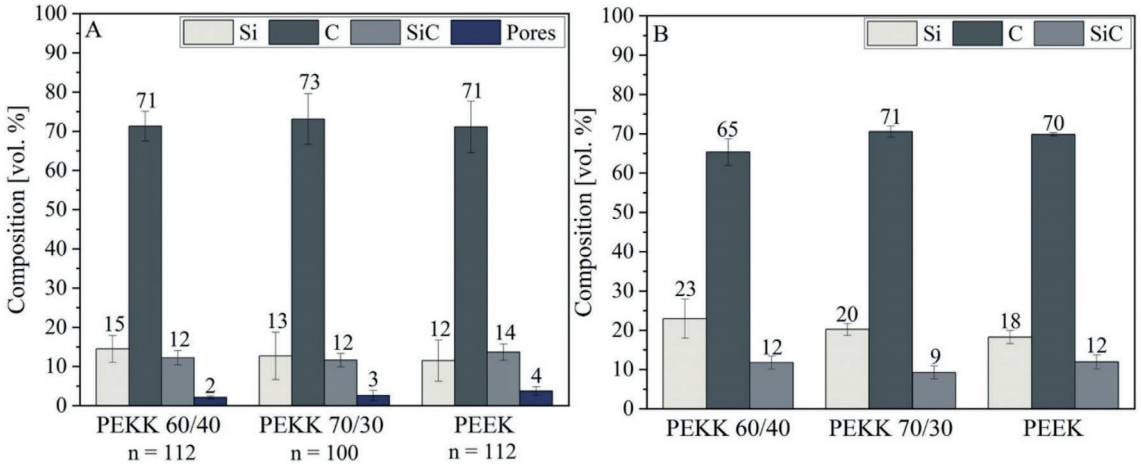

FIGURE 12 | (A) Phase analysis based on deep learning. The amount of carbon consisted of the carbon content of the matrix, carbon fibers in the 0° direction, and carbon fibers in the 90° direction as the output of the deep learning software "Dragonfly". (B) The phase composition according to the combination of oxidation and helium pycnometry.

The amount of silicon was slightly higher when measured by oxidation and helium pycnometry. However, considering the large standard deviation in measured silicon content when using the deep learning program, the results from those two methods did not differ significantly. Thus, the findings achieved by oxidation and helium pycnometry are consistent with results from the deep learning program, in that no relationship between phase composition and matrix precursor was observed for C/C-SiC fabrication. This observation aligns well with similar values concerning bulk density and open porosity of the different thermoplastic-derived C/C-SiC. It is hypothesized that the discussed process-related decrease in plate thickness of PEEK-derived CFRP during pyrolysis negated the effect of increased residual carbon in PEKK-derived C/C, thus leading to similar phase compositions in the C/C-SiC.

3.7 | Three-Point Bending Tests

The flexural strength, Young's modulus and strain to failure were determined from stress–strain curves. Figure 13A shows representative stress–strain curves for PEKK 60/40-, PEKK 70/30- and PEEK-derived C/C-SiC. The flexural strength, strain to failure and Young's modulus values are shown in Figure 13B–D, represented as box plots.

Inspection of Figure 13A revealed differences in the failure behavior of PEEK-, PEKK 60/40-, and PEKK 70/30-derived C/C-SiC. All three C/C-SiC materials exhibited an initial linear-elastic response, followed by non-linear behavior. Peak stresses of PEKK 60/40-derived C/C-SiC were followed by a large stress drop and a stress plateau. By contrast, PEKK 70/30- and PEEK-derived C/C-SiC exhibited a more modest stress drop, followed by a gradual, stepwise decrease in stress.

Values of Young's modulus are shown in Figure 13B. The mean Young's modulus was similar for all three variants of C/C-SiC (39 GPa, 41 GPa and 40 GPa). The standard deviation overlapped the measured values for all three C/C-SiC variants, indicating negligible differences in elastic response. Figure 13C shows the strain to failure values for the three C/C-SiC variants. The mean strain to failure of PEKK 60/40-derived C/C-SiC was 0.62%, slightly greater than that of PEEK-derived C/C-SiC (0.57%) and PEKK 70/30-derived C/C-SiC (0.55%). The mean flexural strength of the PEKK 60/40-derived C/C-SiC, exhibited in Figure 13D, with 223 MPa also was also slightly greater than that of PEEK-derived C/C-SiC (209 MPa) and PEKK 70/30-derived C/C-SiC (205 MPa). Differences in strength and strain to failure between PEEK, PEKK 60/40, and PEKK 70/30 were negligible, given the standard deviations.

3.8 | SEM Analysis

Representative fracture surfaces of PEKK 60/40 (A)-, PEKK 70/30 (B)- and PEEK (C)-derived C/C-SiC after three-point bending tests are shown in Figure 14. The fracture surface of the matrix and the crack progression (III) through the matrix were consistent with a brittle fracture behavior. Inspection of the fiber tows and the fiber-matrix interfaces revealed details of fracture mechanisms. In particular, the images show evidence of fiber-matrix debonding (I), crack progression within the fiber tows (II), single fiber pull-out (IV), as well as partial or complete (multi) fiber pull-out (V). All mechanisms contributed to energy dissipation during crack growth through the composite, increasing the damage tolerance of C/C-SiC composites compared to unreinforced counterparts and have been reported elsewhere [47].

Comparing the fracture images of the three C/C-SiC variants, no obvious differences concerning the fracture behavior were apparent. The similarities in the fracture surfaces indicated similar fiber-matrix bonding. The independence of C/C-SiC fracture surfaces from the polymeric precursor was consistent with results from bending tests, which also showed no relationship between strain to failure, Young's modulus, or flexural strength and the matrix polymer. Thus, the mechanical fracture behavior was, at least to some extent, more affected by factors such as fiber-matrix bonding than by residual mass of polymer after pyrolysis.

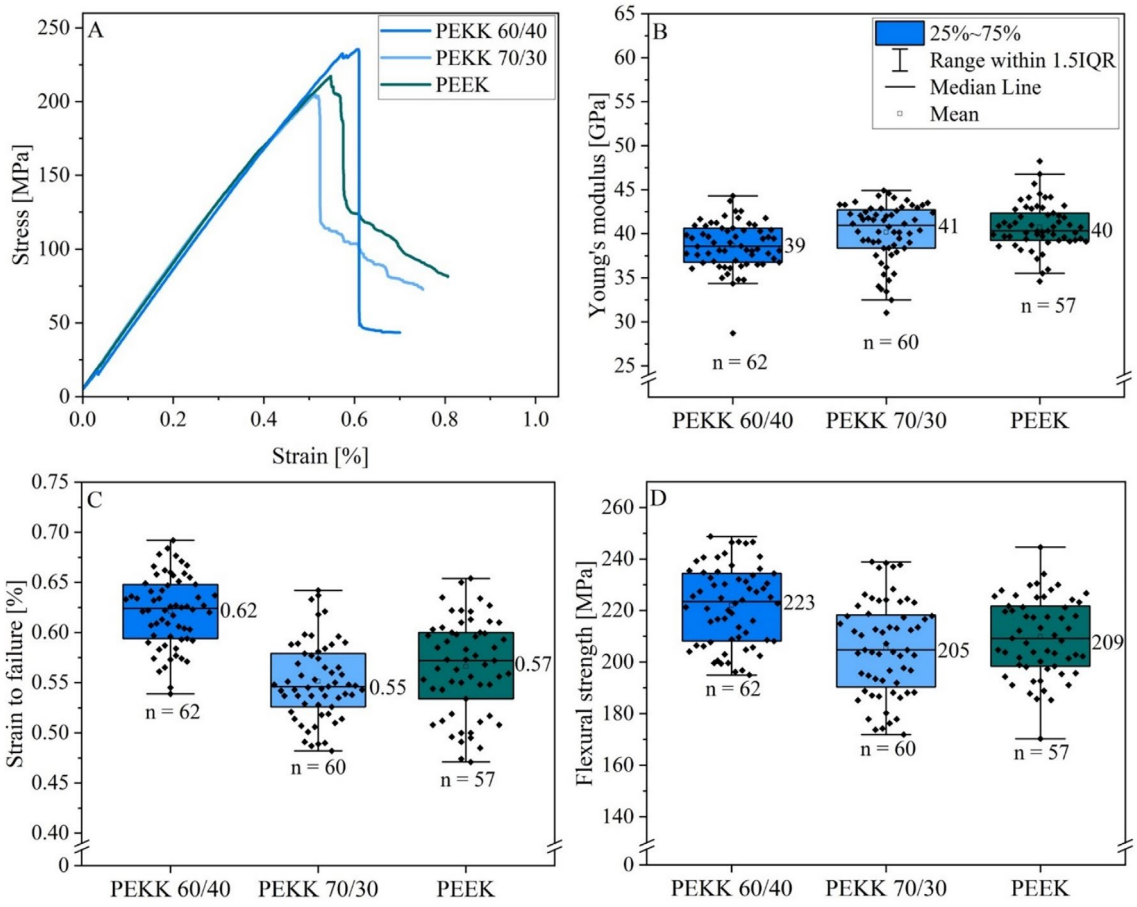

FIGURE 13 | (A) Stress–strain curves for the three C/C-SiC types (B) Young's modulus (C) strain to failure and (D) flexural strength of PEKK 60/40-, PEKK 70/30-, and PEEK-derived C/C-SiC.

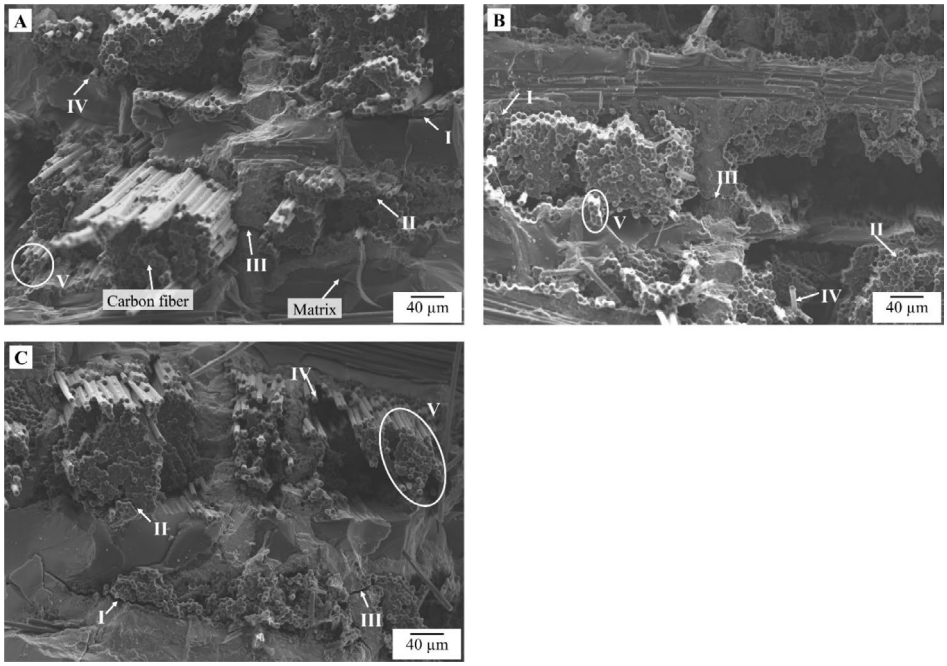

FIGURE 14 | SEM images of (A) PEKK 60/40-, (B) PEKK 70/30-, and (C) PEEK-derived C/C-SiC. Different typical fracture mechanisms for C/C-SiC are highlighted and marked from I–V. (I) Fiber-matrix debonding, (II) crack within fiber tow, (III) matrix crack, (IV) single fiber pull-out, (V) multiple fiber pull-out.

4 | Conclusions

This work showed the first successful fabrication of thermoplastic PEKK-derived C/C-SiC via LSI with excellent mechanical properties and makes PEKK a suitable alternative thermoplastic matrix polymer. PEKK exhibited a higher char yield of > 65% compared to that of PEEK (around 55%). Interestingly, phase composition in the C/C-SiC had similar amounts of carbon, independent of the polymer matrix material. It is hypothesized that process-related different shrinkages of PEEK- and PEKK-derived CFRP during pyrolysis negate the effect of greater char yield in PEKK-derived C/C. To ensure similar plate thickness of the C/C, graphite spacers will be used, and an increased load will be applied during pyrolysis. Nevertheless, mechanical testing proved that the properties of the C/C-SiC materials (flexural strengths above 200 MPa, strain to failures above 0.55% and Young's modulus around 40 GPa) are independent of the polymer material. It is probable that the mechanical properties depend on other factors such as fiber-matrix-bonding (FMB) in the CFRP because FMB influences the crack pattern in the C/C after pyrolysis. The FMB in the CFRP can be measured using nanoindentation. Comparing these results to the crack pattern in the C/C and the mechanical properties in the C/C-SiC allows a closer investigation of the impact of fiber-matrix interaction in the CFRP on processing and final properties of the C/C-SiC. For this work, due to the similar C/C crack patterns and mechanical properties in the C/C-SiC, no differences in the fiber-matrix bonding between PEKK- and PEEK-derived CFRP are expected. Hence, for closer analysis of the FMB and its effect on processing and mechanical properties, the functional groups of the carbon fibers should purposely be altered.

Furthermore, PEKK showed greater crosslinking potential compared to PEEK. One current limitation for establishing thermoplastic-derived C/C-SiC is the lack of form stability due to re-melting of the thermoplastic during pyrolysis. Crosslinking of the CFRP before pyrolysis neglects the re-melting effect, allowing form stability even of complex-shaped components. Thus, crosslinking using PEKK-derived CFRP will be asserted in the future to fabricate complex-shaped C/C-SiC geometries.

Acknowledgments

The authors would like to thank Ute Kuhn from the Department of Polymer Engineering, University of Bayreuth for conducting the DSC measurements.

Conflicts of Interest

The authors declare no conflicts of interest.

References

1. P. Kumar and V. K. Srivastava, "Tribological Behaviour of C/C–SiC Composites—A Review," *Journal of Advanced Ceramics* 5, no. 1 (2016): 1–12, https://doi.org/10.1007/s40145-015-0171-z.

2. P. J. Hofbauer and F. Raether, "Effects of Oxygen on the Liquid Silicon Infiltration (LSI) Process," *Open Ceramics* 14 (2023): 1–10, https://doi.org/10.1016/j.oceram.2023.100337.

3. B. Heidenreich, "C/SiC and C/C-SiC Composites," in *Ceramic Matrix Composites: Materials, Modeling and Technology*, ed. N. P. Bansal and J. Lamon (John Wiley & Sons Inc., 2015).

4. P. Valentine and P. Gradl, *Extreme-Temperature Carbon- and Ceramic-Matrix Composite Nozzle Extensions for Liquid Rocket Engines* (International Astronautical Congress 2019, 2019).

5. S. Flauder, N. Langhof, W. Krenkel, and S. Schafföner, "Size Effect of Carbon Fiber-Reinforced Silicon Carbide Composites (C/C-SiC): Part 1—Bending Load and Statistical Effects," *Journal of the European Ceramic Society* 41, no. 14 (2021): 6805–6814, https://doi.org/10.1016/j.jeurceramsoc.2021.07.040.

6. Y. Peng, Z. Li, A. Li, Q. Wang, R. Bai, and F. Zhang, "Mechanical and Tribological Properties of C/C–SiC Ceramic Composites With Different Preforms," *Science and Engineering of Composite Materials* 30, no. 1 (2023): 1–13, https://doi.org/10.1515/secm-2022-0205.

7. T. K. Schneck, A. Müller, F. Hermanutz, and M. R. Buchmeiser, "Preparation of C/C-SiC Composites From All-Cellulose Precursors," *Macromolecular Materials and Engineering* 304, no. 4 (2019): 1–7, https://doi.org/10.1002/mame.201800763.

8. P. J. Hofbauer, E. Rädlein, and F. Raether, "Fundamental Mechanisms With Reactive Infiltration of Silicon Melt Into Carbon Capillaries," *Advanced Engineering Materials* 21, no. 8 (2019): 1–11, https://doi.org/10.1002/adem.201900184.

9. T. Liensdorf, N. Langhof, and W. Krenkel, "Mechanical Properties of PEEK-Derived C/SiC Composites With Different Fiber Lengths," *Advanced Engineering Materials* 21, no. 5 (2019): 1–9, https://doi.org/10.1002/adem.201800835.

10. G. Krekel, U. J. Zielke, K. J. Hüttinger, and W. P. Hoffman, "The Relevance of the Surface Structure and Surface Chemistry of Carbon Fibres in Their Adhesion to High Temperature Thermoplastics," *Journal of Materials Science* 29, no. 15 (1994): 3984–3992, https://doi.org/10.1007/BF00355958.

11. Y. Cai, S. Fan, H. Liu, et al., "Mechanical Properties of a 3D Needled C/SiC Composite With Graphite Filler," *Materials Science and Engineering A* 527, no. 3 (2010): 539–543, https://doi.org/10.1016/j.msea.2009.08.031.

12. F. Wich, S. Flauder, N. Schneider, et al., "Processing Properties and Pyrolysis Behavior of Novolak-Hexamethylenetetramine Mixtures," *Advanced Manufacturing: Polymer & Composites Science* 9, no. 1 (2023): 1–13, https://doi.org/10.1080/20550340.2023.2187687.

13. F. Reichert, N. Langhof, and W. Krenkel, "Influence of Thermal Fiber Pretreatment on Microstructure and Mechanical Properties of C/C-SiC With Thermoplastic Polymer-Derived Matrices," *Advanced Engineering Materials* 17, no. 8 (2015): 1119–1926, https://doi.org/10.1002/adem.201500193.

14. S. Li, D.-W. Kumar, D.-H. Hwang, S.-Y. Shin, Y.-H. Bae, and Y.-H. Kim, "Geometry and Temperature Effects on Tensile Properties and Failure Behaviors of Open-Hole and Bolted-Joint CF/PEKK Composites," *Composites Part A: Applied Science and Manufacturing* 185 (2024): 1–11, https://doi.org/10.1016/j.compositesa.2024.108336.

15. P. P. Parlevliet, H. E. Bersee, and A. Beukers, "Residual Stresses in Thermoplastic Composites—A Study of the Literature—Part I: Formation of Residual Stresses," *Composites Part A: Applied Science and Manufacturing* 37, no. 11 (2006): 1847–1857, https://doi.org/10.1016/j.compositesa.2005.12.025.

16. J. H. Shin, D. Kim, T. Centea, and S. R. Nutt, "Thermoplastic Prepreg With Partially Polymerized Matrix: Material and Process Development for Efficient Part Manufacturing," *Composites Part A: Applied Science and Manufacturing* 119 (2019): 154–164, https://doi.org/10.1016/j.compositesa.2019.01.009.

17. F. Reichert. Doctoral Thesis (University of Bayreuth, 2018).

18. H. Pérez-Martín, P. Mackenzie, A. Baidak, C. M. Ó Brádaigh, and D. Ray, "Crystallinity Studies of PEKK and Carbon Fibre/PEKK Composites: A Review," *Composites Part B: Engineering* 223 (2021): 1–26, https://doi.org/10.1016/j.compositesb.2021.109127.

19. L. Quiroga Cortés, N. Caussé, E. Dantras, A. Lonjon, and C. Lacabanne, "Morphology and Dynamical Mechanical Properties of Poly Ether Ketone Ketone (PEKK) With Meta Phenyl Links," *Journal of Applied Polymer Science* 133, no. 19 (2016): 1–10, https://doi.org/10.1002/app.43396.

20. K. H. Gardner, B. S. Hsiao, R. R. Matheson, and B. A. Wood, "Structure, Crystallization and Morphology of Poly (Aryl Ether Ketone Ketone)," *Polymer* 33, no. 12 (1992): 2483–2495, https://doi.org/10.1016/0032-3861(92)91128-O.

21. M. Bonmatin, F. Chabert, G. Bernhart, and T. Djilali, "Rheological and Crystallization Behaviors of Low Processing Temperature Poly(Aryl Ether Ketone)," *Journal of Applied Polymer Science* 138, no. 47 (2021): 1–13, https://doi.org/10.1002/app.51402.

22. K. Rashed, A. Kafi, R. Simons, M. Dell'Olio, and S. Bateman, "Polyether Ketone Ketone (PEKK) Matrix Composites for Material Extrusion Additive Manufacturing," *International Journal of Advanced Manufacturing Technology* 130 (2024): 5401–5423, https://doi.org/10.1007/s00170-024-13026-8.

23. M. E. Pomatto and R. B. Moore, "Crystallization Kinetics and Equilibrium Melting Temperature of Poly(Ether Ketone Ketone) With High Terephthalate Content Utilizing Fast Scanning Calorimetry," *Polymer* 271 (2023): 1–9, https://doi.org/10.1016/j.polymer.2023.125810.

24. V. Kishore, C. Ajinjeru, A. A. Hassen, J. Lindahl, V. Kunc, and C. Duty, "Rheological Behavior of Neat and Carbon Fiber-Reinforced Poly(Ether Ketone Ketone) for Extrusion Deposition Additive Manufacturing," *Polymer Engineering & Science* 60, no. 5 (2020): 1066–1075, https://doi.org/10.1002/pen.25362.

25. J. M. Pedroso, M. Enger, P. Bandeira, and F. D. Magalhães, "Comparative Study of Friction and Wear Performance of PEK, PEEK and PEKK Binders in Tribological Coatings," *Polymers* 14, no. 9 (2022): 1–19, https://doi.org/10.3390/polym14194008.

26. W. Freudenberg, F. Wich, J. Best, et al., "Thermo-Oxidative Crosslinking of Carbon Fiber Reinforced PEEK (Polyetheretherketone) for Additive Manufactured Ceramic Matrix Composites," *Advanced Manufacturing: Polymer & Composites Science* 10, no. 1 (2024): 1–13, https://doi.org/10.1080/20550340.2024.2387422.

27. T. Choupin, B. Fayolle, G. Régnier, C. Paris, J. Cinquin, and B. Brulé, "Macromolecular Modifications of Poly(Etherketoneketone) (PEKK) Copolymer at the Melting State," *Polymer Degradation and Stability* 155 (2018): 103–110, https://doi.org/10.1016/j.polymdegradstab.2018.07.005.

28. A. Jonas and R. Legras, "Thermal Stability and Crystallization of Poly(Aryl Ether Ether Ketone)," *Polymer* 32, no. 15 (1991): 2691–2706, https://doi.org/10.1016/0032-3861(91)90095-Z.

29. K. Ramaswamy, V. Modi, P. S. Rao, P. P. Martin, C. T. McCarthy, and R. M. O'Higgins, "An Investigation of the Influence of Matrix Properties and Fibre–Matrix Interface Behaviour on the Mechanical Performance of Carbon Fibre-Reinforced PEKK and PEEK Composites," *Composites Part A: Applied Science and Manufacturing* 165 (2023): 1–15, https://doi.org/10.1016/j.compositesa.2022.107359.

30. M. Coulson, L. Quiroga Cortés, E. Dantras, A. Lonjon, and C. Lacabanne, "Dynamic Rheological Behavior of Poly(Ether Ketone Ketone) From Solid State to Melt State," *Journal of Applied Polymer Science* 135, no. 27 (2018): 1–7, https://doi.org/10.1002/app.46456.

31. N. Jain, M. Kosin, Y. Shi, and D. Koch, "Characterization and Modeling of Transverse Micro-Cracking During Pyrolysis Process of Carbon Fiber Reinforced Plastics," *International Journal of Applied Ceramic Technology* 16, no. 5 (2019): 1734–1743, https://doi.org/10.1111/ijac.13312.

32. S. Flauder, F. Wich, J. Sha, N. Langhof, W. Krenkel, and S. Schafföner, "Effect of Thermo-Mechanical and Low-Cycle Preloading on the Strength of Carbon Fiber-Reinforced Ceramic Matrix Composites," *Journal of the European Ceramic Society* 43, no. 13 (2023): 5474–5483, https://doi.org/10.1016/j.jeurceramsoc.2023.05.037.

33. F. Reichert, N. Langhof, and W. Krenkel, "The Evaluation of Thermoplastic Precursors for C/C-SiC Manufactured by Liquid Silicon Infiltration (LSI)," *Materials Science Forum* 825 (2015): 232–239, https://doi.org/10.4028/www.scientific.net/MSF.825-826.232.

34. J. Yang, Y. Ai, X. Lv, Z. Qi, and J. Jiao, "Fabrication of C/C-SiC Composites Using High-Char-Yield Resin," *International Journal of Applied Ceramic Technology* 18, no. 2 (2021): 449–456, https://doi.org/10.1111/ijac.13655.

35. D. Nestler, N. Nier, K. Roder, et al., "Development and Characterisation of Phenolic Resin Moulding Materials for the Production of New Short Fibre-Reinforced C/C-SiC Composites," *Materials Science Forum* 825 (2015): 215–223, https://doi.org/10.4028/www.scientific.net/MSF.825-826.215.

36. T. Opel, N. Langhof, and W. Krenkel, "Development and Tribological Studies of a Novel Metal-Ceramic Hybrid Brake Disc," *International Journal of Applied Ceramic Technology* 19, no. 1 (2022): 62–74, https://doi.org/10.1111/ijac.13826.

37. B. Vieille, A. Coppalle, L. Le Pluart, et al., "Influence of a Flame-Retardant on the Fire-Behaviour and the Residual Mechanical Properties of C/PEKK Composite Laminates Exposed to a Kerosene Flame," *Composites Part A: Applied Science and Manufacturing* 152 (2022): 1–16, https://doi.org/10.1016/j.compositesa.2021.106720.

38. C. Croshaw and W. Jeffrey, "Thermal Degradation of Poly (ether ketone ketone) Copolymers at Processing Temperatures," 2021 SAMPE neXus Proceedings, 2021, Virtual Event, https://digitallibrarynasampe.org/data/pdfs/s2021_pdfs/TP21-0000000450.pdf.

39. K. L. White, L. Jin, N. Ferrer, M. Wong, T. Bremner, and H.-J. Sue, "Rheological and Thermal Behaviors of Commercial Poly(Aryletherketone)s," *Polymer Engineering & Science* 53, no. 3 (2013): 651–661, https://doi.org/10.1002/pen.23309.

40. G. J. Farrow, G. H. Wostenholm, M. I. Darby, and B. Yates, "Thermal Expansion of PEEK Between 80 and 470K," *Journal of Materials Science: Materials in Electronics* 9, no. 6 (1990): 743–744, https://doi.org/10.1007/BF00721820.

41. C. Pradere and C. Sauder, "Transverse and Longitudinal Coefficient of Thermal Expansion of Carbon Fibers at High Temperatures (300–2500 K)," *Carbon* 46, no. 14 (2008): 1874–1884, https://doi.org/10.1016/j.carbon.2008.07.035.

42. R. Krueger and A. Bergan, "Advances in Thermoplastic Composites Over Three Decades—A Literature Review," 2024 NASA STI Program Report Series, Langley Research Center, https://ntrs.nasa.gov/api/citations/20240005376/downloads/NASA-TM-20240005376.pdf.

43. F. Gao, J. W. Patrick, and A. Walker, "The Characterisation of Cracks and Voids in Two-Dimensional Carbon-Carbon Composites," *Carbon* 31, no. 1 (1993): 103–108, https://doi.org/10.1016/0008-6223(93)90162-4.

44. S. Flauder, N. Langhof, and W. Krenkel, "Tailored Macro-Pores During the Formation of C/C-SiC via Liquid Phase Pyrolysis," *Journal of the European Ceramic Society* 41, no. 5 (2021): 2995–3001, https://doi.org/10.1016/j.jeurceramsoc.2020.10.006.

45. T. K. Schneck, B. Brück, M. Schulz, et al., "Carbon Fiber Surface Modification for Tailored Fiber-Matrix Adhesion in the Manufacture of C/C-SiC Composites," *Composites Part A: Applied Science and Manufacturing* 120 (2019): 64–72, https://doi.org/10.1016/j.compositesa.2019.02.021.

46. J. Dai, Z. Zhang, Y. Zu, and J. Sha, "Role of Fiber–Matrix Adhesion at CFRP Stage on Microstructure and Mechanical Properties of C/C–SiC Composite," *International Journal of Applied Ceramic Technology* 19, no. 1 (2022): 79–90, https://doi.org/10.1111/ijac.13923.

47. P. León-Pérez, T. Opel, G. Puchas, et al., "Effect of the Fibre Volume Content on the Machinability and Surface Integrity in Grinding C/C-SiC Composites," *Journal of the European Ceramic Society* 45, no. 6 (2025): 1–15, https://doi.org/10.1016/j.jeurceramsoc.2024.117173.